chemosensors

MDPI

Article

A NO_2 Sensitive MnO_2/Graphene Oxide Composite Based Gas Sensor

Mohamed Ayoub Alouani [1,2,3], Juan Casanova-Chafer [4], Santiago de Bernardi-Martín [5], Alejandra García-Gómez [5], Xavier Vilanova [1,2,3,*] and Eduard Llobet [1,2,3,*]

1 MINOS, School of Engineering, Universitat Rovira i Virgili, Avda. Països Catalans 26, 43007 Tarragona, Spain
2 IU-RESCAT, Research Institute in Sustainability, Climatic Change and Energy Transition, Universitat Rovira i Virgili, Joanot Martorell 15, 43480 Vila-seca, Spain
3 TecnATox—Centre for Environmental, Food and Toxicological Technology, Universitat Rovira i Virgili, Avda. Països Catalans 26, 43007 Tarragona, Spain
4 Material Nova, Université de Mons, Place du Parc 23, 7000 Mons, Belgium; juan.casanovachafer@umons.ac.be
5 Gnanomat, C/Faraday 7, 28049 Madrid, Spain; santiago.bernardi@gnanomat.com (S.d.B.-M.); alejandra.garcia@gnanomat.com (A.G.-G.)
* Correspondence: xavier.vilanova@urv.cat (X.V.); eduard.llobet@urv.cat (E.L.)

Abstract: Nanosized manganese dioxide (MnO_2) material has been successfully incorporated into a graphene oxide (GO) sensitive layer. Since this type of heterojunction has never been reported in the literature related to gas sensing, these sensors were prepared, tested, and reported. The morphological properties and composition of the MnO_2@GO material have been thoroughly studied via FESEM, XRD, Raman spectroscopy, HR-TEM, and ATR-IR. Gas sensitivity and selectivity towards mainly NO_2 and other gases (NH_3, CO, ethanol, benzene, and H_2) have also been studied. The obtained sensors were exposed to different concentrations of NO_2 ranging from 200 ppb to 1000 ppb at 150 °C and under close to real conditions (25% relative humidity and 70% relative humidity). The MnO_2@GO sensors have shown a high response of 16.3% towards 1 ppm of NO_2 under dry conditions and a higher response of 44% at 70% RH towards the same concentration. Finally, it has also shown a strong sensitivity for NO_2.

Keywords: graphene oxide; manganese dioxide; gas sensor; NO_2 detection; humidity

Received: 4 February 2025
Revised: 4 March 2025
Accepted: 6 March 2025
Published: 8 March 2025

Citation: Alouani, M.A.; Casanova-Chafer, J.; de Bernardi-Martín, S.; García-Gómez, A.; Vilanova, X.; Llobet, E. A NO_2 Sensitive MnO_2/Graphene Oxide Composite Based Gas Sensor. *Chemosensors* **2025**, *13*, 96. https://doi.org/10.3390/chemosensors13030096

1. Introduction

The detection and monitoring of nitrogen dioxide (NO_2, annual exposure limit: 5 ppm) [1] is critical for environmental protection and human health. Prolonged exposure to this gas, even at low concentrations, can have detrimental effects, ranging from respiratory problems to fatalities [2,3]. As industries grow, particularly in urban environments, there is a pressing need for efficient and reliable gas-sensing technologies that can operate in real time and under varying environmental conditions [4]. For this reason, this field of research is advancing rapidly with the continuous emergence of materials with high sensitivity to the target toxic gases, and thus, many studies report high-performance sensors. Some of the latest works are by Chummei et al. where they studied the performance of iron oxyhydroxide as a NO_2 gas sensor. This sensor showed a response of 36% towards 37 ppb of NO_2 at 160 °C [5]. Another newly reported work by Evans et al. is a bismuth-based metal–organic framework (Bi-MOF)-derived Bi_2Se_3. For this sensor, the response towards 500 ppb of NO_2 at room temperature was 32.1% [6]. Moreover, a 2D Tellurene-based sensor has been studied as a NO_2 gas sensor at room temperature. This novel 2D material has shown a good response of 35% towards sub-ppm concentrations of NO_2 and a fast response

of 14 s [7]. Finally, a TiO_2-based sensor where the titanium dioxide is used as a membrane to a transparent ordered micro-hollow-bump structure to produce a MEMS was fabricated and studied as a NO_2 gas sensor by Yu-Ming et al., the gas sensing tests were operated at room temperature under UV-light activation and the reported response towards 4 ppm of NO_2 was 9.5% with average response and recovery times of 7 s and 144 s, respectively [8].

Graphene-based chemoresisitve gas sensors have also gained huge recognition because of the remarkable properties of graphene, which include large surface area, thermal stability, high carrier mobility, and tuneable electrical properties by the adsorption of gas molecules [9].

Graphene oxide (GO) is a derivative of graphene, usually obtained by chemical oxidation of a multilayer graphite via the most common method (Hummer's method) [10]. Moreover, the GO surface is rich in oxygen-containing groups, which enhance gas sensing performance [11]. Many previous works focused on the sensing performance of GO, mainly towards NO_2. For example, Park et al. have explored the sensing properties of GO prepared via a modified Hummer's method towards 5 ppm of NO_2 at 150 °C, the sensor showed a response of 32% [12]. Moreover, Ali A-J et al. synthesized GO via a modified Hummer's method and deposited it on a glass substrate via a spin coating technique, which was later used for gas detection tests of 100 ppm of NO_2 at 200 °C and showed a response of 12% [13]. Finally, Vien et al. successfully obtained GO from an upcycled plastic waste via chemical and thermal treatments, and this obtained graphene oxide was used to detect 1 ppm of NO_2 at room temperature with a response of 11% [14].

Although pristine GO has been an excellent choice for gas sensing detection, it still has some limitations in selectivity and sensitivity, particularly for detecting low concentrations of different gases, especially NO_2. Hence, GO-MO_X heterojunctions have emerged. These are obtained via the controlled incorporation of metal oxides into the GO layer to enhance sensitivity towards different target gases. Some of the reported metal oxide candidates for the enhancement of the GO gas sensing properties are ZnO [15], In_2O_3 [16], V_2O_5 [17], SnO_2 [18], and Co_3O_4 [19].

Similarly, MnO_2 has been investigated independently in gas sensors because of its advantages, which are high catalytic activity, redox potential, low toxicity, and high stability. Manganese dioxide has been utilized in different fields, such as biomedical [20], energy storage [21], and gas sensing [22]. Focusing on the sensing utility of MnO_2, it was used separately for NO_2 detection as reported by Pritamkumar et al., where they have hydrothermally grown α-MnO_2 mesoporous cubes of several nanocrystals and had a response of 33% towards 100 ppm of NO_2 at 150 °C [23]. Moreover, Ahmad et al. have also tested hydrothermally grown α-MnO_2 as ethanol gas sensors; they had a response of 30.6 towards 200 ppm of the target gas at 300 °C [24]. Additionally, Kumar R. et al. have explored the sensing properties of MnO_2 nanofibers as ammonia gas sensors and reported a response of 1.5% towards 1 ppm of NH_3 [25]. Furthermore, manganese dioxide was also studied as a response enhancement agent for gas-sensitive materials, it was reported in the literature that it was incorporated in different materials such as polymers [26,27], nanocomposites (SnO_2/MnO_2) [28], NiO nanosheets (NiO@MnO_2) [29], ZnO (ZnO/MnO_2) [30], and finally in graphene-based materials such as graphene [31] and reduced graphene oxide (rGO) [32–35].

Since the incorporation of MnO_2 into GO creating a MnO_2/GO composite for gas sensing purposes was not studied before, and since MnO_2 has been reported previously to work successfully as a gas properties enhancer in graphene-based materials, it is believed that the synergy between GO and MnO_2 in heterojunction sensors can lead to an enhancement in both the sensitivity and selectivity of GO towards toxic gases especially NO_2, as

MnO_2 can provide active sites for gas adsorption, while GO facilitates charge transfer and signal amplification.

For this reason, this paper aims to investigate the sensing performance of MnO_2@GO nanocomposite sensors for detecting mainly NO_2 and other gases such as NH_3, CO, ethanol, benzene, and H_2, focusing on their sensitivity and selectivity. The effects of varying the sensor operating conditions on performance are also examined to optimize these sensors for practical environmental monitoring applications.

2. Materials and Methods

2.1. Preparation of MnO_2/GO Composite

MnO_2/GO composite (MnO_2/GO 10/90 wt.%) was synthesized using a process based on patented procedures [36] (Patent number ES2678419A1). Briefly, GO provided by Grapheneall was dispersed in oxalic acid, in which the starting Mn_3O_4 had been previously dissolved at 50 °C. After homogenization, MnO_2 nanomaterials were slowly precipitated on GO by adding NaOH solution under vigorous agitation. The solid was filtered and dried overnight at room temperature. Finally, the sample was pulverized into a fine powder. Synthesis parameters, such as temperature, stirring speed, addition rate, or MnO_2/GO proportion, were controlled to obtain the desired crystallinity that provides the material with optimal properties. It is worth noting that the MnO_2 content (10 wt.%) in GO was determined via thermogravimetric analysis (TGA) using a sample mass of 2.0–2.5 g. The analysis was conducted from an initial temperature of 40 °C to a final temperature of 1050 °C, with a heating rate of 10 °C/min. Air was used as the carrier gas at a flow rate of 100 mL/min. The MnO_2 percentage in the sample corresponds to the residual mass at the end of the thermogravimetric analysis, as graphene oxide undergoes complete thermal decomposition at this temperature, leaving only the metallic oxide as a residue.

2.2. Material Preparation and Deposition

A total amount of 10 mg of MnO_2@GO powder was initially suspended in 10 mL of ethanol and then sonicated for 30 min for a proper homogenization of the obtained suspension. Later, the MnO_2@GO suspension was deposited on top of commercially available interdigitated electrodes (deposited already on an alumina substrate (Al_2O_3) obtained from CeramTec, Plochingen, Germany) via a spray coating technique. During the deposition process, the temperature was fixed at a degree of 60 °C for the attempt to evaporate the ethanol to obtain a clean and homogenous sensitive layer with good adhesion onto the substrate. The previously mentioned substrate dimensions and shape are shown in detail in Figure 1; the substrate contains interdigitated platinum electrodes on the top side and a platinum heater on the bottom to help reach the desired temperature for the gas properties tests. The width of the fingers shown in the figure is 0.216 mm, and the gap between them is 0.3 mm.

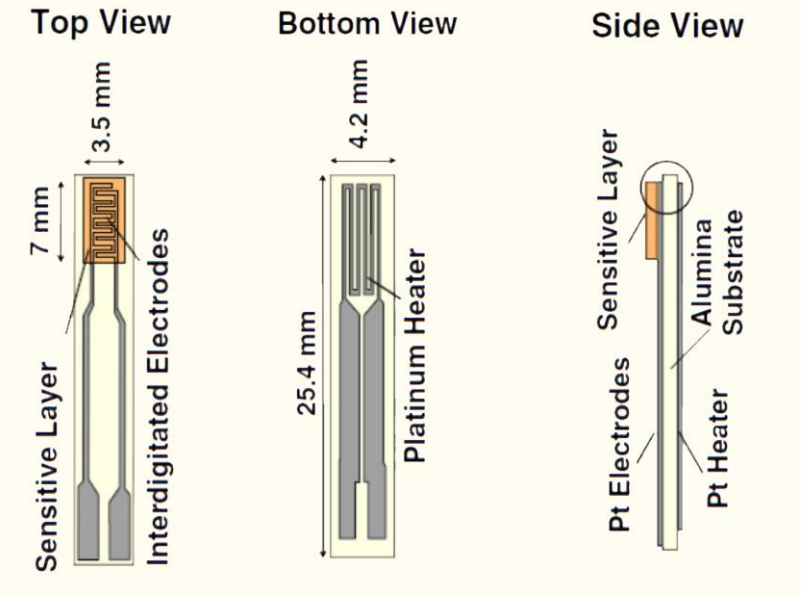

Figure 1. Different sides view the used alumina substrate with the platinum electrodes and heater.

2.3. Material Characterization and Gas Sensing Measurements

To investigate the various morphological and sensing features of the synthesized materials, a variety of characterization approaches were employed. Using XRD, the crystalline phases of the graphene and manganese oxide were identified. The measurements were taken with a Bruker-AXS D8-Discover (Ettingen, Germany) diffractometer that had a GADDS (general area diffraction system), a vertical $\theta-\theta$ goniometer, a parallel incident beam (Gobel mirror), and an XYZ motorized stage to produce Cukα radiation, the X-ray diffractometer was run at 40 kV and 40 mA. It was also run at ambient temperature in increments of 0.05° in the 2θ range from 0° to 80°. The ATR-IR investigation of the interaction between the molecules of the MnO_2@GO material was carried out using a Jasco FTIR/IR-6700 (Tokyo, Japan) infrared spectrometer equipped with a diamond crystal kit. The distribution and morphology of nanosized materials were examined using a Carl Zeiss AG-Ultra 55 (ZEISS, Jena, Germany) Field Emission Scanning Electron Microscope (FESEM). Using a JEOL F200 TEM ColdFEG (Tokyo, Japan) running at 200 kV, high-resolution transmission electron microscopy (HRTEM) characterization was carried out. Utilizing a Gatan OneView camera (Plesanton, CA, USA), a CMOS-based and optical fiber-coupled detector with 4096 by 4096 pixels, electron diffraction patterns were obtained for the HR-TEM images. The (S)TEM pictures were processed using the Gatan Digital Micrograph application. With a camera length of 200 mm, STEM pictures (1024 $\times$ 1024 pixels) were captured from the JEOL bright-field (BF) and high-angle annular dark-field (HAADF) detectors. A JEOL beryllium double-tilt holder for energy-dispersive X-ray spectroscopy (EDS) was used to hold the samples. An EDS Centurio detector (silicon drift) with an effective size of 100 mm^2 and an energy resolution of 133 eV was used to record STEM-EDS mapping. The JEOL Analysis program was used to process STEM-EDS maps (512 $\times$ 512 pixels) in order to verify the form of the nanosized MnO_2 and its integration in the graphene layers. Last, a Raman spectrometer (Renishaw, plc., Wotton-under-Edge, UK) was utilized to evaluate the materials' crystallinity using a green laser with a wavelength of 514 nm. The manufactured sensors were put inside a Teflon container with a volume of 35 cm^3. A continuous flow of dry air (Air Premier, 99.995% purity) and additional target analytes diluted at varying percentages were then passed through the Teflon chamber using a set of Bronkhorst (Ruuurlo, The Netherlands) mass-flow controllers. Calibrated bottles containing the initial dilutions of the gases (NO_2-1 ppm, CO-100 ppm, NH_3-100 ppm, ethanol-20 ppm, benzene-10 ppm,

and H_2-1000 ppm balanced in dry air) were used to achieve the required concentrations of the gases. An Agilent HP 34972A (Santa Clara, CA, USA) multimeter was used to record resistance changes in real-time. To assess the impact of ambient moisture on sensor responses, a controller evaporator mixer (CEM) was used to achieve low humidity levels of 25% relative humidity. When the relative humidity reached 70%, a bubbling water system was used to humidify the dry airflow with the matching gas concentration. The inability of the CEM system to sustain a consistent humidity level above 50% RH led to the selection of the bubbling water system.

The sensing response is defined as the relative change in resistance and was calculated using this formula for oxidizing gases:

$$R\ (\%) = ((R_g - R_a)/R_a) \times 100$$

The following formula for reducing gases:

$$R\ (\%) = ((R_a - R_g)/R_a) \times 100$$

where R_g and R_a correspond, respectively, to the resistance values prior to and following gas exposure [37].

Exposure and recovery times are generally defined as the time needed for the sensor to reach saturation after exposure to the target gas and the time taken to recover 90% of its initial baseline, respectively. These values were calculated and reported in the supporting information file under Figure S8 and Table S1.

Moreover, the limit of detection (LOD) is the lowest concentration of target gas that can be distinguished from the common atmosphere, which produces a signal greater than three times the standard deviation of the noise level. Theoretical LOD was calculated following this formula:

$$LOD = 3.3 \times (Sy/S)$$

where Sy is the standard deviation of the response of the curve and (S) is the slope of the calibration curve at different concentrations. The Sy and S values were obtained from the plotted curves using Excel; the calculated values were compiled in Table S2.

Additionally, I-V curve measurements were conducted on the MnO_2@GO composite to check whether we have heterojunction or not; the result of the measurement is shown in Figure S9.

Finally, the system used consists of a set of mass flows that allows the control of the flow of synthetic air and the percentage of dilution of the target gas. The outlets of the mass flows are connected to the inlet of the already described chamber in the previous part. The chamber is connected to an Agilent multimeter, which allows the display of the resistance changes in real-time using the appropriate software. The schematic representation of the gas detection process and equipment used is already shown in previous works [32].

3. Results

Initially, this section deliberates on the obtained morphological characterization results of the MnO_2@GO sensitive layer via XRD, Raman, FESEM, HR-TEM, and ATR-IR techniques. Later, NO_2 gas responsiveness of the layer at 150 °C under dry conditions was tested and reported alongside tests at different levels of relative humidity. Additionally, selectivity tests are conducted and reported. Finally, the gas sensing mechanism of the NO_2 gas adsorption is presented and explained.

3.1. Gas Sensitive Layer Characterization

3.1.1. XRD

To identify and quantify the crystalline phase of the manganese oxide present in the powder, XRD analysis was conducted. Figure 2a shows the XRD diffractogram of pristine GO, and Figure 2b shows the diffractogram of the MnO_2@GO material. The blue lines in both figures correspond to the peaks of GO material in positions 2θ = 11° and 2θ = 43° following the JCPDS card number 00-065-1528. It is noticed in Figure 2a that the peak of GO at 2θ = 11° is intense and sharp since the pristine GO initially has good crystallinity, and in Figure 2b, the same peak became less intense and less sharp following the incorporation of the MnO_2 nanosized material which modified the crystallinity of the pure GO. Since Mn_2O_4 and MnO_2 have the same Mn to O ratio and cubic structure, JCPDS card number 01-073-5018 was used to identify the peaks of the nanosized MnO_2 and is shown with the red lines. One major specific peak is shown in the position of 2θ = 19° proving the presence and the crystalline phase of the nanosized material; another peak should appear at 2θ = 45° but taking into consideration the angle of contact of the XRD measurement and the low concentration of the material, this peak is not intense.

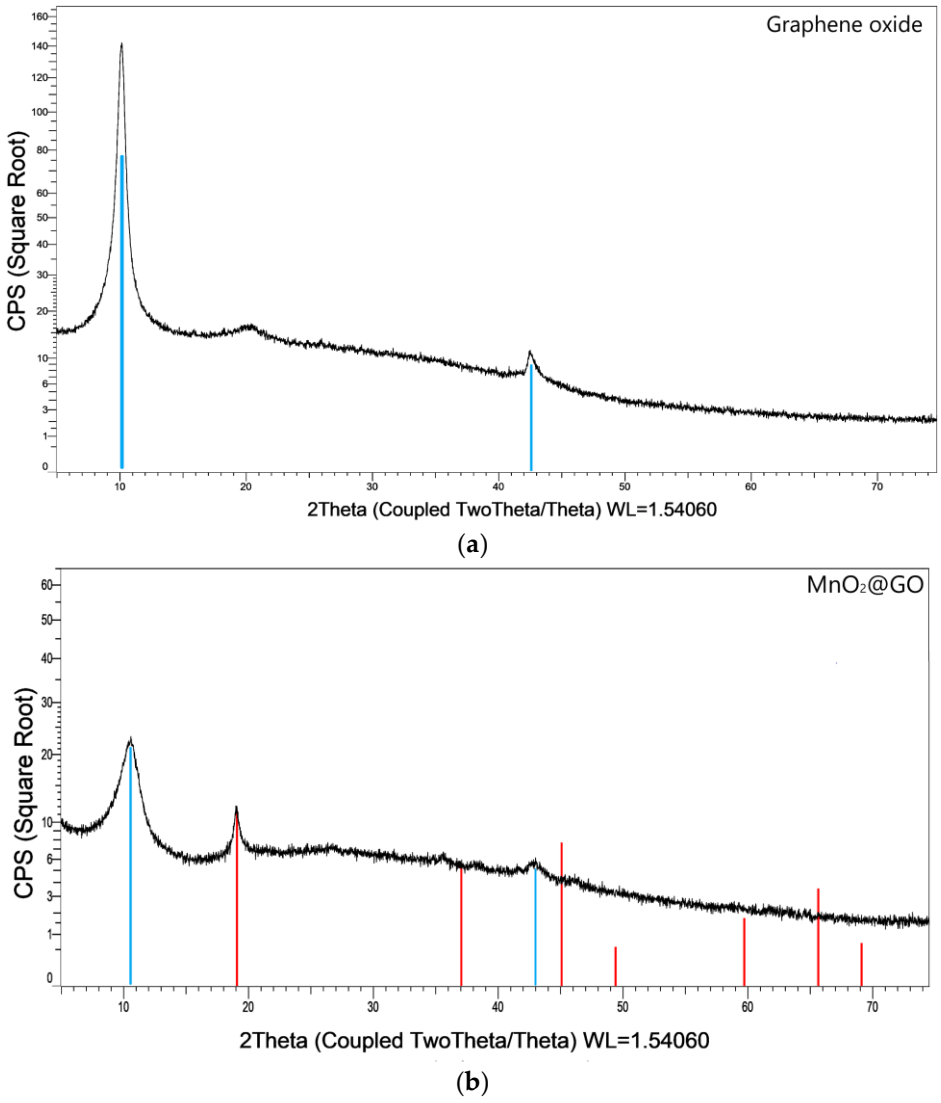

Figure 2. XRD diffractograms of (**a**) Pristine GO and (**b**) MnO_2@GO powder showing the presence and crystalline phase of manganese oxide. Blue and red lines correspond to the GO and MnO_2 reference peaks, respectively.

3.1.2. Raman

Raman spectroscopy can be employed to investigate the molecular structure of carbon materials and assess imperfections and disorders in the substance. Figure 3a,b show the Raman spectra of bare GO and GO incorporated with MnO_2 nanomaterial, respectively. Two unique peaks consistently appear in the analysis of graphene-based materials: the D-band and the G-band. The primary characteristic, located around 1600 cm^{-1}, pertains to the first-order scattering of the E_2g phonons at the Brillouin zone center and originates from the in-plane motion of sp^2 carbon atoms [38]. In our case, this peak is located at 1590 cm^{-1}, regardless of whether the GO contains MnO_2. At the same time, the D-band appears around 1340 cm^{-1} and indicates the formation of j-point photons with A_1g symmetry associated with double C=C bonds, suggesting that a more intense band corresponds to an increased number of sp^2 domains. In our case, this specific band appears around 1355 cm^{-1} for both materials. Moreover, the strength of the D-band peak is greatly affected by the presence of disorders and defects, including vacancies, edges within the carbon lattice, and grain boundaries [39]. To evaluate the degree of reduction and disorder of the GO, a straightforward calculation of the intensity ratio of the D and G band peaks (I_D/I_G) is adequate [40]. The I_D/I_G calculation for both materials is 0.94 for pristine GO and 0.90 for MnO_2@GO, and according to Ferrari's classification, since the ratios are below 3.5, it means that the materials have a very low degree of disorder [41].

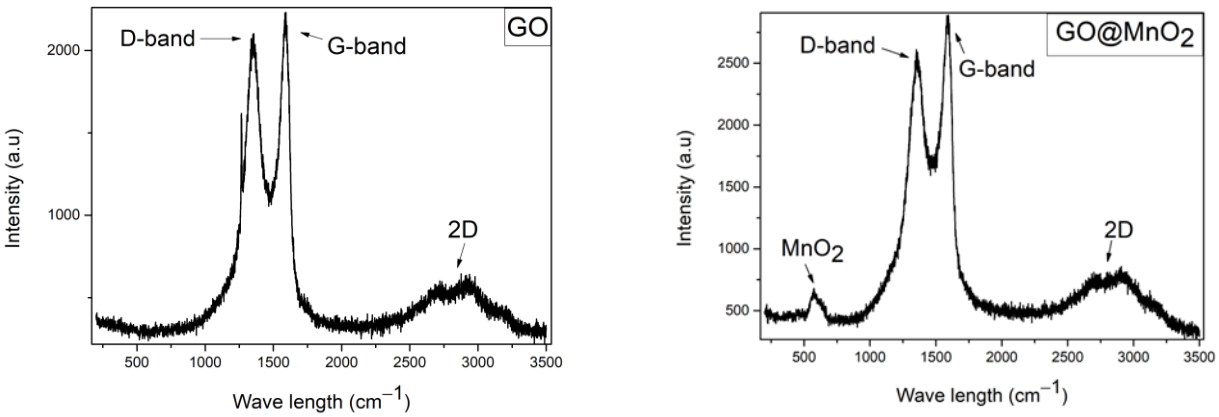

(**a**) (**b**)

Figure 3. Raman spectrum of (**a**) pristine GO and (**b**) MnO_2@GO nanomaterial.

Ultimately, the second-order bands can be seen between 2500 cm^{-1} and 3200 cm^{-1}, featuring a consistently observable peak near 2700 cm^{-1}, referred to as the 2D band. They are typically employed to identify the number of layers of the graphene because of graphene's tendency to stack [42]. As shown in Figure 3a,b, a visible bump-like peak corresponding to the 2D band is also present between 2600 cm^{-1} and 3200 cm^{-1}.

The only difference between the two graphs is the presence of a distinct peak at around 600 cm^{-1}, as can be seen in Figure 3b which has been reported in the literature before as being indicative of the presence of MnO_2 [43].

3.1.3. FESEM

Figure 4a,b shows FESEM images of the layers of bare GO and MnO_2@GO deposited on the surface of the alumina substrates, respectively, seen via a back-scattering detector. The only difference between the two figures is the voltage used when taking the images; for pristine GO, it was 15 kV (Figure 4a), and for MnO_2@GO, it was 5 kV (Figure 4b) due to the inability to acquire clear images of the MnO_2/GO composite layer using the same voltage because of the inclusion of nanosized MnO_2 makes the material more conductive. Figure 4a

shows pristine GO wrinkled sheets-like morphology. Kasimayan U. et al. showed a similar morphology of pristine GO via FESEM [44]. Meanwhile, Figure 4b shows a homogeneous MnO_2@GO layer, where the surface of the sensor is rich with bright spots corresponding to the MnO_2 that can be seen as well dispersed all over the layer. We can also notice the presence of some agglomerations of this metal oxide, insinuating the successful formation of the MnO_2@GO heterojunction. The thickness of the different layers was checked, and Figures S1–S3 show the layer preparation for the cross-section process.

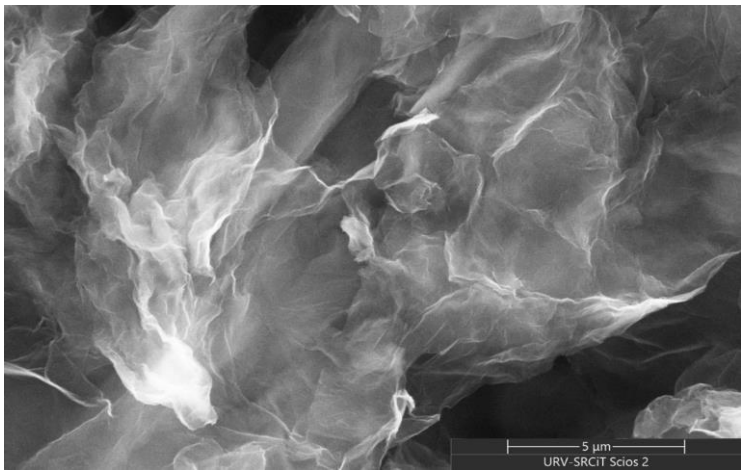

(**a**)

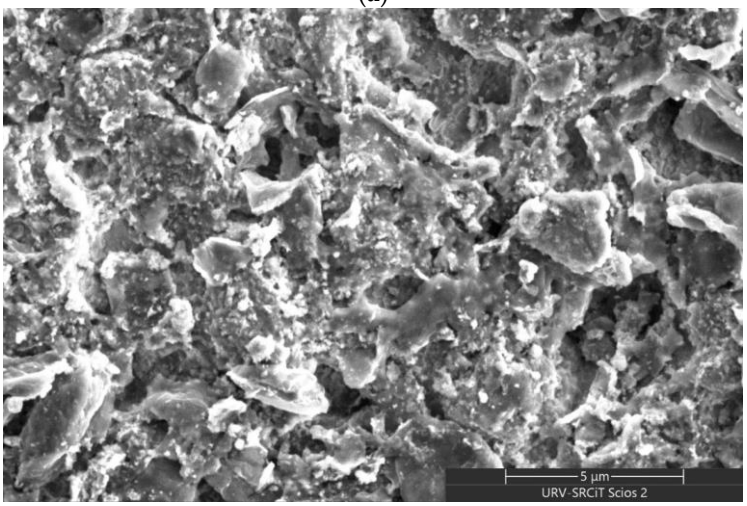

(**b**)

Figure 4. FESEM images of (**a**) pristine GO layer deposited on top of the alumina substrate and (**b**) MnO_2@GO sensitive layer deposited on the same type of substrate.

3.1.4. HR-TEM

HR-TEM analysis was conducted to examine better the morphology of the MnO_2 nanomaterial and its incorporation in the graphene layer. Figure 5a shows the HR-TEM image of bare GO material showing graphene sheets on top of each other. Figure 5b shows the MnO_2@GO layer showing the presence of a different material in the dark, which corresponds to the MnO_2. The EDS analysis shown in Figure 5c exhibits needle-like shaped manganese oxide alongside a cluster of small MnO_2 dots forming aggregates in bright color. The mapping of the same area (Figure 5d) shows the distribution of Mn material. EDS mapping of the same area for the other elements present in the layer, which are carbon and oxygen, are shown also in Figure 5e,f. Meanwhile, Figure 5g shows an overlapping image of all the elements present in the same EDS image with MnO_2 nanosized material having a light purple color because of the mixture of blue and red colors of Mn and O elements.

The obtained result from this analysis proves the successful incorporation of MnO_2 into the GO material.

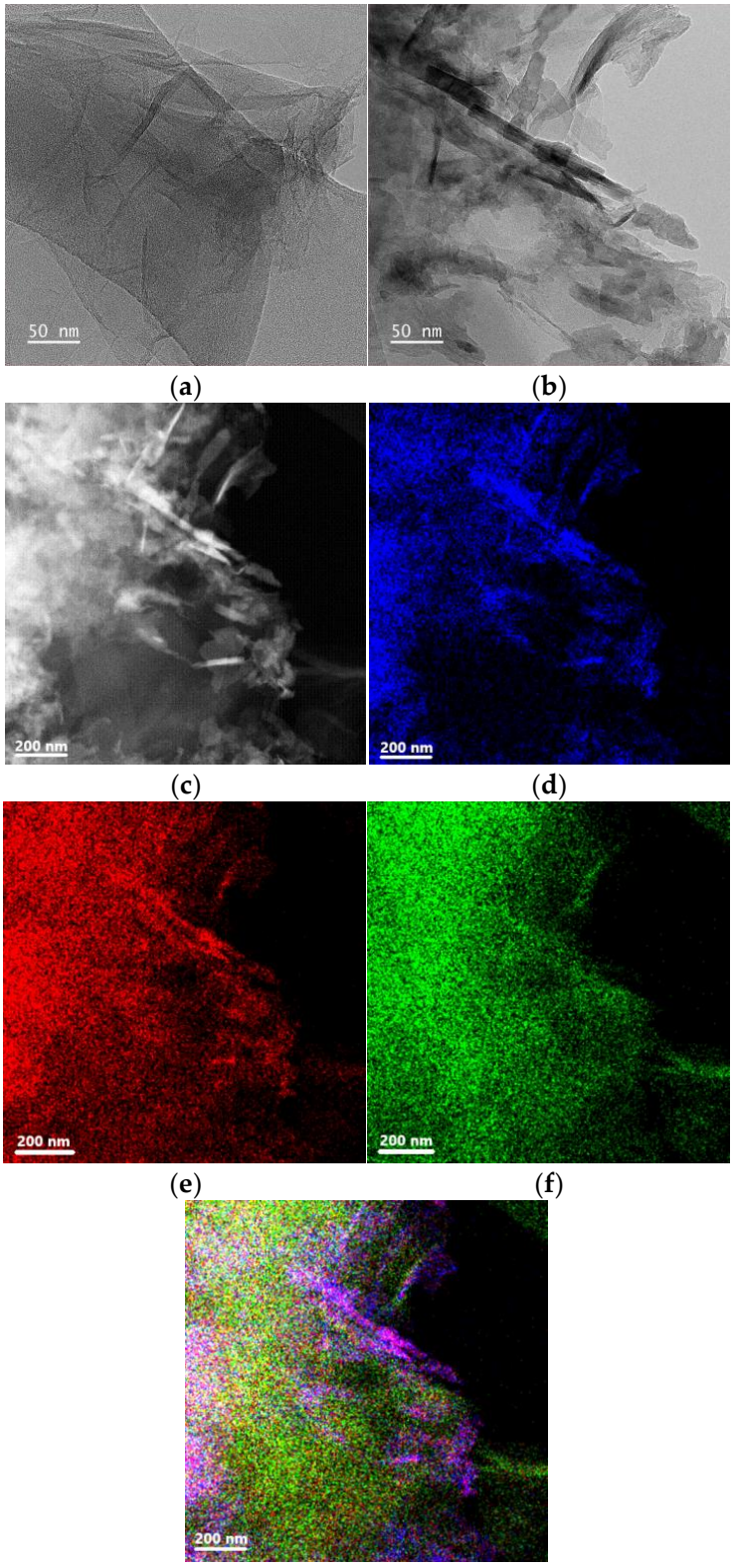

Figure 5. (**a**) HRTEM image of Pristine GO (**b**) HRTEM image of MnO_2@GO, (**c**) EDS analysis image of the chosen area, (**d**) EDS mapping image of the same area of Mn element (**e**) EDS map of O element in the same mapped area (**f**) EDS map of C element in the same mapped area and (**g**) Overlay image of all the maps of the elements C, O and Mn.

3.1.5. ATR-IR

Figure 6a,b show the ATR-IR spectra of pristine GO and MnO_2@GO, respectively. Figure 6a shows GO characteristic peaks at around wavenumbers 1580 cm^{-1}, 1408 cm^{-1}, 1044 cm^{-1} and a bump-like peak between 2600 cm^{-1} and 3600 cm^{-1}, corresponding to C=C, carbonyl C=O, epoxy C=O, and OH groups, respectively. Meanwhile, in the ATR-IR spectra of MnO_2@GO represented in Figure 6b, it is seen that the same pristine GO peaks are present with a slight shift (lower wavenumbers), as well as specific Mn=O stretching vibration band at around 490 cm^{-1}, alongside the stretch of hydrated MnO_2, which is found at around 1120 cm^{-1} [45].

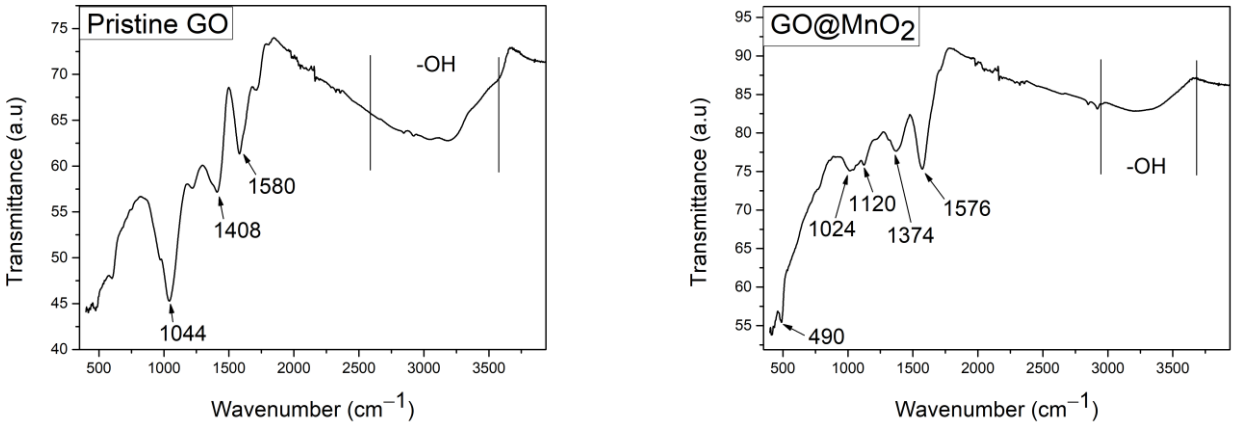

Figure 6. ATR-IR spectra of (**a**) pristine GO and (**b**) MnO_2@GO sensitive layers.

3.2. Gas Sensing Results

A selection of different gases was utilized to investigate the sensing properties of the pristine GO and MnO_2@GO sensors. First, NO_2 was thoroughly studied with different dilutions ranging from 200 ppb to 1000 ppb under dry air as well as under ambient moisture conditions (close to real conditions) at 150 °C. The choice of the working temperature was based on the fact that for room temperature, 50 °C, and 100 °C, our sensors have shown a baseline resistance producing (Overload, OVLD) because of the high resistance values that our acquisition systems cannot measure properly. When working at 150 °C, they showed the baseline resistance values shown in Figure 7b and in Figures S4–S7 in the supporting information file. This temperature is the lowest one, allowing the resistance to be measured properly. In addition, in a previous work conducted by Carlo C. et al., they tested a range of different operating temperatures from 25 °C to 200 °C using GO as a NO_2 sensor and showcased the highest sensitivity and selectivity at 150 °C [46]. Figure 7a shows the response of the different sensors towards different concentrations of NO_2 and at different levels of humidity. The sensors showed an increase in responses with an increase in the analyte concentration independently of the atmosphere conditions. In dry conditions, the MnO_2@GO sensor shows a 4-fold better response at 1 ppm of NO_2 than the pristine GO sensor. When introducing moisture to the gas test process, it was observed that the response of the pristine GO sensor slightly increased going from dry to 25% RH, and basically, it did not change when increasing RH% to 70%. This behavior was studied and explained by Maurizio D. et al., who stated that the response of pristine GO towards NO_2 slightly increased when proceeding from dry conditions to low relative humidity levels and was almost unaffected by higher levels of RH [47]. In fact, graphene oxide is rich in oxygen functional groups that play the role of active sites for the adsorption of water molecules. Depending on the morphological and chemical composition of the synthesized graphene oxide, the GO layer can be easily saturated, even at low levels of

relative humidity. In addition, the working conditions of 150 °C can have a role in the early saturation of the GO layer since it can cause its reduction, thus reducing the number of oxygen functional groups on its surface. Moreover, adding MnO_2 notably increases the sensor response for all humidity ranges. For instance, at 25% RH, the responses of the MnO_2@GO sensor increased significantly, reaching 34.5% at 1 ppm of NO_2, which is 5-fold higher than the pristine GO sensor response values, while at 70% RH, the response of the MnO_2@GO sensor kept increasing significantly and rapidly throughout the range of the NO_2 concentrations reaching a maximum of 44% at 1 ppm of NO_2 which is almost 7-folds the response of the pristine GO sensor at the same concentration. Nevertheless, as can be seen, the response of the MnO_2@GO sensor is much more affected by humidity. While the pristine GO shows an increase in the response in the presence of water vapor, the increase from 25% to 70% of relative humidity does not result in significant changes in the sensor response. Moreover, the MnO_2@GO sensor response is highly affected by the concentration of water vapor, which means that to be operated in real conditions, it should be operated with a humidity sensor to compensate for this dependence on humidity. Figure 7b shows the resistance changes in the MnO_2@GO sensor when exposed to 1 ppm of NO_2 at 70% RH; it is worth noting that a slight drift was noticed in the baseline and was corrected using specific software. As can be seen, the composite behaves as a p-type sensing layer, decreasing the layer's electrical resistance when exposed to the oxidizing NO_2. Response to the other dilutions of NO_2 (200–400–600–800 ppb) is shown in Figures S4–S7 in the support information. Exposure and recovery times calculated for the gas test are presented in Figure S8 in the supporting information file; the best values are 878 s and 994 s, respectively, when exposed to 1 ppm of NO_2, and the values for all the other dilutions of NO_2 are presented in Table S1. The theoretical values for the limits of detection were also calculated and compiled in Table S2. The MnO_2@GO sensor reached a LOD of 251 ppb under dry conditions, 385 ppb under 25% RH, and 341 ppb under 70% RH, all at 150 °C.

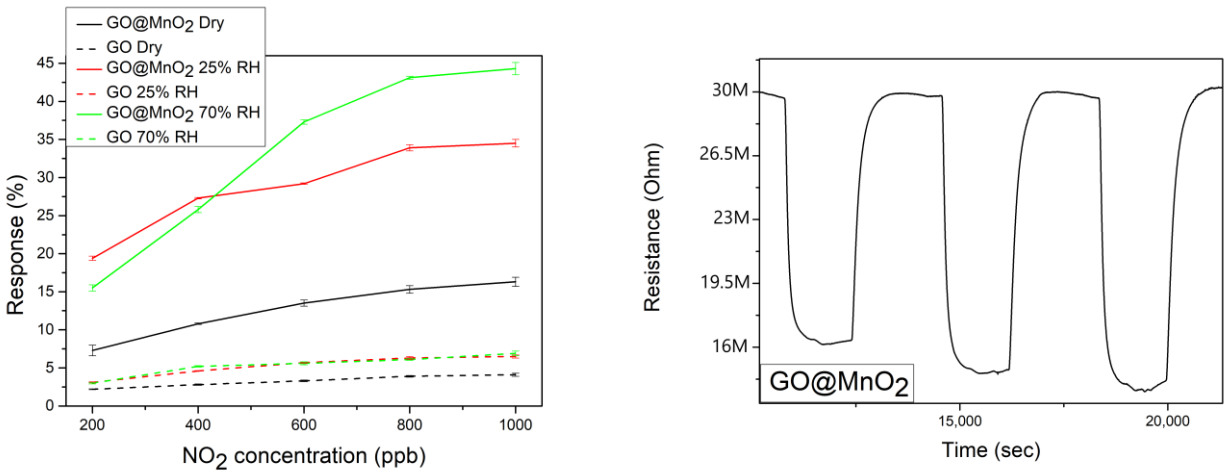

Figure 7. Calibration curve of the responses of (**a**) pristine GO and MnO_2@GO sensors towards different concentrations of NO_2 at 150 °C and under dry and humid conditions (**b**) resistance changes in the MnO_2@GO for 1000 ppb of NO_2 at 70% RH.

To check the selectivity of the sensors, we have measured the response of the sensors under dry air at 150 °C exposed to NH_3 (50 ppm), CO (50 ppm), ethanol (20 ppm), benzene (1 ppm), and H_2 (500 ppm). The selection of these gases was based on different criteria; for example, ammonia is very toxic and present almost everywhere in the environment. Carbon monoxide and nitrogen dioxide are usually present in some combustion processes, and both have to be measured in air quality monitoring applications. Since ethanol vapors are

colorless, volatile, and highly flammable, the detection of ethanol vapors in the atmosphere is important for avoiding fire/explosion risks as well as risks to human health. Ethanol has also been reported in the literature as a target species for GO-based gas sensors [48]. Benzene is a very cancerogenic gas and graphene-based materials have been used for the specific detection of this gas [49]. Finally, H_2 is a flammable substance, and the early detection of hydrogen leaks in facilities such as chemical plants is crucial to save lives; in the literature, it was reported that GO was doped with Pd to create specific H_2 sensors [50].

As shown in Figure 8, both pristine GO and MnO_2@GO sensors show no response to hydrocarbons (benzene and ethanol). Pristine GO showed more sensitivity toward ammonia rather than to NO_2, with responses of 5.6% and 4.1%, respectively. When incorporating nanosized MnO_2 into the pristine GO, the MnO_2@GO sensitive layer showed a significant increase in the response towards NO_2; meanwhile, the response to ammonia decreased in comparison to pristine GO with responses of 16.3% for NO_2 and 3.2% for ammonia. Including MnO_2 also increased the response to CO and H_2, although the increase was much lower than the achieved for NO_2. Summarizing the inclusion of MnO_2 in the GO leads to a more sensitive sensor towards NO_2.

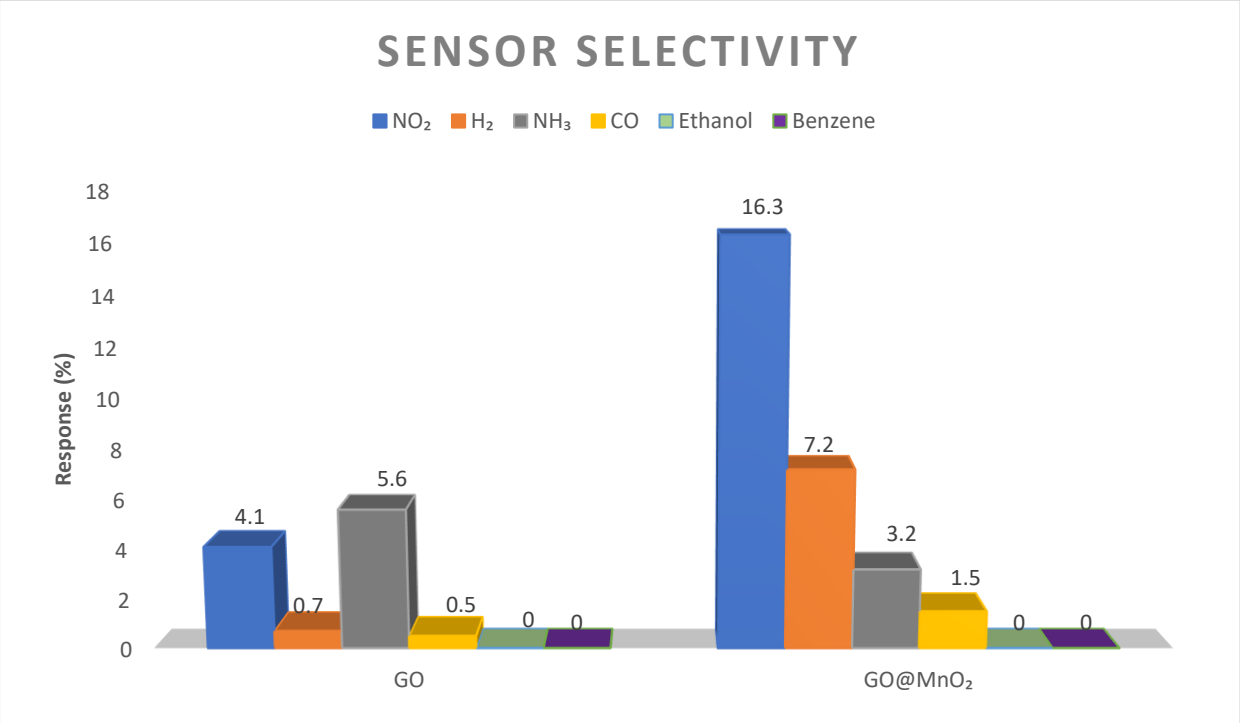

Figure 8. Comparison of the responses of the different sensors towards different gases under dry conditions to study the selectivity of the sensitive layer.

Table 1 contains data obtained from previous works using individually pristine GO, GO-based composites with different MO_X species, and pristine MnO_2 alongside some hybrids of MnO_2 with different materials (graphene-based, polymers) to make NO_2 gas sensors. In this work, the reported NO_2 responses were generally higher than the ones reported in the literature. Most of the previous works used relatively high concentrations of the target gas; meanwhile, in this work, the NO_2 concentrations reached low ppb levels. While most works did not explore the response variation in their materials under different ambient humidity levels, our material has been reported to detect NO_2 in different relative humidity levels and has showcased very high responses.

Table 1. Comparison of the responses of MnO_2@GO sensors with previously reported works in the literature.

Material	NO_2 Concentration (ppm)	Response (%)	Condition	Sensitivity (%ppm^{-1})	T (°C)	Ref
Upcycled GO Nanosheets	1.03	11	Dry	NA *	RT	[14]
Hydrogel-Based Colorimetric Sensor	100	1	Dry	NA	RT	[51]
Flexible gas sensor based on Ceria (CeO_2) nano-cube decorated rGO	70	52.84	Dry	NA	RT	[52]
rGO-ZrO_2 Hybrid	5	15.8	Dry	NA	RT	[53]
GO/$SrTiO_3$	1	3.2	Dry	2.9	100	[54]
direct-ink-writing of eco-friendly GO	1	1.68	Dry	NA	150	[55]
hydrothermally grown α-MnO_2 mesoporous cubes	100	33	Dry	NA	150	[23]
polythiophene-MnO_2	100	90	RH	NA	75	[26]
Nano-MnO_2/xanthan	7	1.21	Dry	0.17	RT	[27]
δ-MnO_2-Epitaxial Graphene-Silicon Carbide Heterostructures	5	0.27	55% RH	0.14	RT	[31]
MnO_2 doped rGO	1	6.2	Dry	9.8	RT	[32]
Pristine GO	1	4.1	Dry	2.5	150	This work
MnO_2@GO	1	16.3	Dry	11.3	150	This work
MnO_2@GO	1	44	70% RH	37.5	150	This work

* NA: not available.

3.3. Proposed Sensing Mechanism

The sensing mechanism in MnO_2@GO heterojunction involves the interaction between the sensing layer (the hybrid material) and gas molecules such as NO_2. This mechanism relies on changes in the electrical conductivity or resistance of the material when exposed to NO_2 gas, driven by the distinct properties of both graphene oxide and manganese dioxide.

NO_2 is an electron-withdrawing gas, functioning as an oxidizing agent. When NO_2 molecules interact with the MnO_2@GO p-n heterojunction, they adsorb onto the surface of the sensing layer. The presence of oxygen-containing groups on the surface of GO creates active sites for the target gas molecules, thus extracting electrons from the hybrid material surface [56]. This increases the hole concentration, causing a decrease in resistance because of the p-type behavior of GO, where holes are the primary charge carriers.

MnO_2, an n-type metal oxide, is known for its strong catalytic properties; thus, it enhances the adsorption of NO_2 molecules by providing active sites for the gas molecules. When in contact with ambient air, MnO_2 initiates a chemisorption of oxygen molecules, resulting in the creation of oxygen species that capture electrons from the conduction band of the material and result in the creation of a thin depletion layer [52]. The previously mentioned process causes an increase in the baseline resistance of the sensor because of the development of a large potential barrier [57]. Depending on the working temperature, different oxygen groups such as O^-, $O_2{}^-$ O^{2-} can be formed; since we are working at an operating temperature of 150 °C, O^- is formed following these reactions [23]:

$$O_2 \text{ gas} \rightarrow O_2 \text{ (ads)}$$

$$O_2^- + e^- \rightarrow 2O^- \text{ (ads)}$$

Later, when exposed to NO_2 gas, the previously adsorbed oxygen species interacts with the target gas molecules, releasing electrons back to the materials conduction band, thus decreasing the depletion layer size and subsequently decreasing the baseline resistance. This explained process is shown in Figure 9, where MnO_2 and GO band gap values were taken from previous works that have studied these materials' electrical properties thoroughly [58,59]. The following reactions describe the previously explained process:

$$NO_2 \text{ (gas)} + e^- \rightarrow NO_2^- \text{ (ads)}$$

$$NO_2^- \text{ (ads)} + O^- \text{ (ads)} + 2e^- \rightarrow NO \text{ (gas)} + 2O^- \text{ (ads)}$$

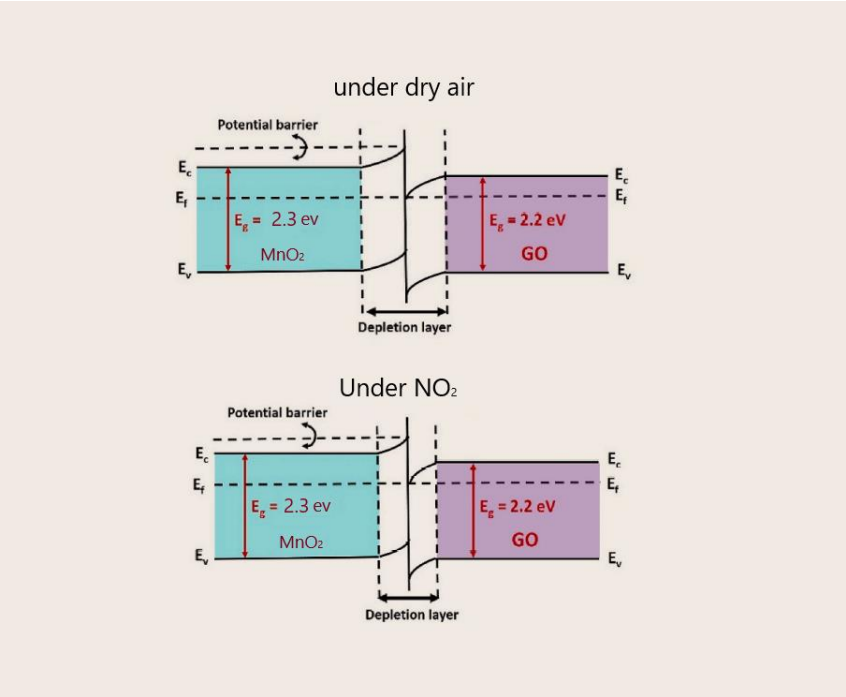

Figure 9. Schematic representation of the depletion layer formation and potential barrier development under air and when in contact with the target gas (NO_2).

In our case, the resistance changes in the MnO_2@GO p-n heterojunction sensing material are in alignment with the proposed mechanism since its baseline resistance decreases when in contact with NO_2 gas and is seen to recover when there is no contact with the target gas.

The performance of gas sensors, including MnO_2@GO hybrids, can vary in the presence of humidity due to its impact on adsorption and desorption processes. Water molecules from humid air tend to adsorb on the GO surface, forming a thin layer of hydroxyl groups. These hydroxyl groups can interact with NO_2 enhancing the response of the sensors. Under low humidity, more NO_2 molecules can be adsorbed on the surface, but at high humidity, the adsorbed water molecules may block active sites, and competition between them and NO_2 molecules takes place [60]. However, MnO_2's catalytic properties can help mitigate this effect by promoting the dissociation of water molecules, allowing NO_2 molecules to continue interacting with the sensor surface [61], which explains the significant increase in the response of the MnO_2@GO sensor with an increase in the humidity level shown in this work.

4. Conclusions

This study reports the incorporation of MnO_2 into GO for gas sensing applications, which was unprecedented in this field. A successful incorporation of nanosized MnO_2 into GO takes place. Morphological and compositional characterizations such as XRD, Raman, FESEM, HR-TEM, and ATR-IR were used to prove the previous statement. Moreover, gas sensing tests were conducted to study the sensitivity and selectivity of the fabricated sensor towards NO_2 gas. The MnO_2@GO sensor exhibited high responses toward different dilutions of the target gas even at low concentrations of 200 ppb at a working temperature of 150 °C. Ambient moisture was also introduced in the gas sensing process, and it was noticed that it enhanced the responses of the MnO_2@GO sensor. Finally, the sensitive material showed a very high sensitivity towards NO_2 compared to other tested gases such as NH_3, CO, ethanol, benzene, and H_2. Compared to previously reported works in the literature of pristine GO, Pristine MnO_2, and other MO_X-GO materials, our fabricated sensor showed better responses at lower concentrations of NO_2. Additionally, they have shown good long-term stability during a period of continuous tests of 8 months. All these results make MnO_2@GO nanomaterial an excellent and reliable NO_2 chemoresistive detector to be introduced in real-life monitoring of this gas.

Supplementary Materials: The following supporting information can be downloaded at: https://www.mdpi.com/article/10.3390/chemosensors13030096/s1, Figure S1: Cross-section of the pristine GO layer; Figure S2: Cross-section of the MnO_2@GO layer; Figure S3: Cross-section of the MnO_2@GO layer with indication to the layers deposited using the ion bean and electron beam; Figure S4: Resistance changes in the MnO_2@GO sensor when exposed to 200 ppb of NO_2 under 70% RH 150 °C; Figure S5: Resistance changes in the MnO_2@GO sensor when exposed to 400 ppb of NO_2 under 70% RH 150 °C; Figure S6: Resistance changes in the MnO_2@GO sensor when exposed to 600 ppb of NO_2 under 70% RH 150 °C; Figure S7: Resistance changes in the MnO_2@GO sensor when exposed to 800 ppb of NO_2 under 70% RH 150 °C; Figure S8: Exposure and recovery times of the same sensor at different concentrations of NO_2 under 70% RH at 150 °C; Table S1: Exposure and recovery times of the MnO_2@GO sensor when exposed to different concentrations of NO_2 under 70% RH at 150 °C; Table S2: Calculated theoretical values of LOD for the different sensors at different conditions; Figure S9: I-V curve measurement performed on the MnO_2@GO composite.

Author Contributions: Conceptualization, X.V. and J.C.-C.; methodology, M.A.A. and X.V.; validation, M.A.A.; formal analysis, M.A.A., X.V. and J.C.-C.; investigation, M.A.A.; resources, S.d.B.-M. and A.G.-G.; data curation, M.A.A.; writing—original draft preparation, M.A.A.; writing—review and editing, J.C.-C., E.L., X.V., S.d.B.-M. and A.G.-G.; visualization, M.A.A.; supervision, J.C.-C. and X.V.; project administration, X.V. and E.L.; funding acquisition, X.V. and E.L. All authors have read and agreed to the published version of the manuscript.

Funding: Grant PID2022-142451OB-C21 funded by MICIU/AEI/10.13039/501100011033 and by "ERDF/EU" and grant no. 2021 SGR 00147 funded by AGAUR. E.L. is supported by the Catalan Institute for Advanced Studies (ICREA) via the 2023 Edition of the ICREA Academia Award. J.C.-C. is supported by the Marie Skłodowska-Curie grant agreement No. 101066282—GREBOS. M.A.A. is supported by MICINN grant agreement PRE2019-087854.

Institutional Review Board Statement: Not applicable.

Informed Consent Statement: Not applicable.

Data Availability Statement: Data used in this paper is available upon demand.

Acknowledgments: The authors want to acknowledge Sergi Plana Ruiz for his help and important discussions about the HR-TEM analysis results, Mariana Stefanova Trifonova for her assistance in the FESEM images preparation, Eric Pedrol Ripoll for his help with the Raman analysis and Fransesc Guisper Guirado for his help with the XRD analysis.

Conflicts of Interest: The authors declare no conflicts of interest. GNANOMAT was not a funding sponsor for this study and had not a role in the design of the study nor on the decision to publish the results.

References

1. Beloconi, A.; Vounatsou, P. Revised EU and WHO Air Quality Thresholds: Where Does Europe Stand? *Atmos. Environ.* **2023**, *314*, 120110. [CrossRef]
2. Huang, S.; Li, H.; Wang, M.; Qian, Y.; Steenland, K.; Caudle, W.M.; Liu, Y.; Sarnat, J.; Papatheodorou, S.; Shi, L. Long-Term Exposure to Nitrogen Dioxide and Mortality: A Systematic Review and Meta-Analysis. *Sci. Total Environ.* **2021**, *776*, 145968. [CrossRef]
3. Latza, U.; Gerdes, S.; Baur, X. Effects of Nitrogen Dioxide on Human Health: Systematic Review of Experimental and Epidemiological Studies Conducted between 2002 and 2006. *Int. J. Hyg. Environ. Health* **2009**, *212*, 271–287. [CrossRef] [PubMed]
4. Milone, A.; Monteduro, A.G.; Rizzato, S.; Leo, A.; Di Natale, C.; Kim, S.S.; Maruccio, G. Advances in Materials and Technologies for Gas Sensing from Environmental and Food Monitoring to Breath Analysis. *Adv. Sustain. Syst.* **2023**, *7*, 2200083. [CrossRef]
5. Shangguan, C.; Xu, K.; Dong, M.; Ren, G.; You, R.; Liu, Z.; Ou, R.; Lu, L.; Hu, Y.; Ma, Q.; et al. Two-Dimensional Iron Oxyhydroxide for Visible-Light-Driven NO_2 Sensing. *ACS Appl. Nano Mater.* **2025**, *8*, 952–961. [CrossRef]
6. Kibet, E.; Dong, Y.; Yu, Y.; Niu, W.; Tan, Y.; Liu, H.; Hao, J.; Qu, W.; Zhou, Y.; Hu, W.; et al. Formation of Nanoporous Bi_2 Se_3 by Selenization of Bismuth Metal–Organic Frameworks for Highly Sensitive and Selective NO_2 Sensing at Room Temperature. *ACS Appl. Nano Mater.* **2025**, *8*, 1233–1244. [CrossRef]
7. Je, Y.; Chee, S.-S. High-Speed and Sub-Ppm Detectable Tellurene NO_2 Chemiresistive Room-Temperature Sensor under Humidity Environments. *Electron. Mater. Lett.* **2025**, *21*, 94–101. [CrossRef]
8. Yeh, Y.-M.; Chang, S.-J.; Fang, S.-Y.; Hsueh, T.-J. TiO_2-based nitrogen dioxide gas sensor with transparent ordered micro-hollow bump structure prepared by 3D heterogeneous integration technology. *Mater. Sci. Semicond. Process.* **2024**, *184*, 108832. [CrossRef]
9. Novoselov, K.; Geim, A.; Morozov, S.; Jiang, D.; Zhang, Y.; Dubonos, S.; Grigorieva, I.; Firsov, A. Electric field effect in atomically thin carbon films. *Science* **2004**, *306*, 666–669. [CrossRef]
10. Jiříčková, A.; Jankovský, O.; Sofer, Z.; Sedmidubský, D. Synthesis and Applications of Graphene Oxide. *Materials* **2022**, *15*, 920. [CrossRef]
11. Choi, Y.; Yoon, Y.-G.; Choi, K.S.; Kang, J.H.; Shim, Y.-S.; Kim, Y.; Chang, H.; Lee, J.-H.; Park, C.; Kim, S.Y.; et al. Role of Oxygen Functional Group in Graphene Oxide for Reversible Room-Temperature NO_2 Sensing. *Carbon* **2015**, *91*, 178–187. [CrossRef]
12. Park, J.; Kim, Y.; Park, S.; Sung, S.; Jang, H.; Park, C. Band Gap Engineering of Graphene Oxide for Ultrasensitive NO_2 Gas Sensing. *Carbon* **2020**, *159*, 175–184. [CrossRef]
13. Al-Jawdah, A.; Aljarrah, R.; Al-Khaykanee, M.; Skof, M. Enhance The Gas-Sensing Performances Of Graphene Oxide (GO) Thin Films For Detecting Nitrogen Dioxide Gas. *Al-Qadisiyah J. Pure Sci.* **2021**, *26*, 432–443. [CrossRef]
14. Trinh, V.; Xu, K.; Yu, H.; Ha, N.; Hu, Y.; Khan, M.W.; Ou, R.; Luan, Y.; Zhang, J.; Ma, Q.; et al. Upcycled Graphene Oxide Nanosheets for Reversible Room Temperature NO_2 Gas Sensor. *Chemosensors* **2024**, *12*, 108. [CrossRef]
15. Natarajamani, G.S.; Kannan, V.; Madanag, S. Synergistically Enhanced NH_3 Gas Sensing of Graphene Oxide-Decorated Nano-ZnO Thin Films. *Mater. Chem. Phys.* **2024**, *316*, 129036. [CrossRef]
16. Han, J.; Gu, G.; Gao, Y.; Yu, N.; Zhou, W.; Wang, Y.; Kong, D.; Gao, Y.; Lu, G. Prototype Alarm Integrating Pulse-Driven Nitrogen Dioxide Sensor Based on Holey Graphene Oxide/In_2O_3. *ACS Sens.* **2024**, *9*, 5425–5435. [CrossRef] [PubMed]
17. Srivastava, S.; Singh, A.; Sahz, M.; Yadav, B.; Pandey, N. Development of V_2O_5@GO (1D/2D) Nanohybrid Based Chemiresistor for Low-Trace of Toluene. *Sens. Actuators B Chem.* **2023**, *400*, 134817. [CrossRef]
18. Amoh, P.; Elwardany, A.; Fujii, M.; Hassan, H. Room Temperature-Built Gas Sensors from Green Carbon Derivative: A Comparative Study between Pristine SnO_2 and GO-SnO_2 Nanocomposite. *J. Nano Res.* **2024**, *82*, 77–94. [CrossRef]
19. Mohammad-Yusof, N.; Rozali, S.; Ibrahim, S.; Siddick, S. Synthesis of Hybridized Fireworks-like Go-Co_3O_4 Nanorods for Acetone Gas Sensing Applications. *Mater. Today Commun.* **2023**, *35*, 105516. [CrossRef]
20. Wu, M.; Hou, P.; Dong, L.; Cai, L.; Chen, Z.; Zhao, M.; Li, J. Manganese Dioxide Nanosheets: From Preparation to Biomedical Applications. *Int. J. Nanomed.* **2019**, *14*, 4781–4800. [CrossRef]
21. Sarma-Choudhury, S.; Katiyar, N.; Saha, R.; Bhattacharya, S. Inkjet-Printed Flexible Planar Zn-MnO_2 Battery on Paper Substrate. *Sci. Rep.* **2024**, *14*, 1597. [CrossRef] [PubMed]
22. Malook, K.; Khan, H.; Shah, M.; ul-Haque, I. Highly Selective and Sensitive Response of Polypyrrole-MnO_2 Based Composites towards Ammonia Gas. *Polym. Compos.* **2018**, *40*, 1676–1683. [CrossRef]
23. Shinde, P.V.; Xia, Q.X.; Ghule, B.G.; Shinde, N.M.; Seonghee, J.; Kim, K.H.; Mane, R.S. Hydrothermally Grown α-MnO_2 Interlocked Mesoporous Micro-Cubes of Several Nanocrystals as Selective and Sensitive Nitrogen Dioxide Chemoresistive Gas Sensors. *Appl. Surf. Sci.* **2018**, *442*, 178–184. [CrossRef]

24. Umar, A.; Ibrahim, A.; Kumar, R.; Albargi, H.; Zeng, W.; Alhmami, M.; Alsaiari, M.; Baskoutas, S. Gas Sensor Device for High-Performance Ethanol Sensing Using α-MnO_2 Nanoparticles. *Mater. Lett.* **2021**, *286*, 129232. [CrossRef]
25. Kumar, R.; Kushwaha, N.; Kumar, R.; Mittal, J. Ammonia Gas Sensing Using Thin Film of MnO_2 Nanofibers. *IEEE Sens. J.* **2016**, *16*, 4691–4695. [CrossRef]
26. Shirgaonkar, D.; Yewale, M.; Shin, D.K.; Mathad, S.; Nakate, N.T.; Ahmad, R.; Pawar, S.; Al Kahtani, A.; Aftab, S. High Selectivity in NO_2 Gas Sensing Applications Using Polythiophene-MnO_2 Composite Thin Films. *Sens. Actuators Phys.* **2024**, *377*, 115740. [CrossRef]
27. Fahmy, A.; Saeed, A.; Dawood, U.; Abdelbary, H.; Altmann, K.; Schönhals, A. Nano-MnO_2/Xanthan Gum Composite Films for NO_2 Gas Sensing. *Mater. Chem. Phys.* **2022**, *296*, 127277. [CrossRef]
28. Fan, G.; Huo, F.; Guan, J.; Yu, H.; Zhu, Q.; Han, N.; Mo, J.; Chen, Y. MnO_2 Enhanced Low Temperature HCHO Sensing Performance of SnO_2. *Sens. Actuators B Chem.* **2024**, *412*, 135803. [CrossRef]
29. Li, C.; Choi, P.; Masuda, Y. Highly Sensitive and Selective Gas Sensors Based on NiO/MnO_2@NiO Nanosheets to Detect Allyl Mercaptan Gas Released by Humans under Psychological Stress. *Adv. Sci.* **2022**, *9*, 2270174. [CrossRef]
30. Xie, C.; Xiao, L.; Hu, M.; Bai, Z.; Xia, X.; Zeng, D. Fabrication and Formaldehyde Gas-Sensing Property of ZnO–MnO_2 Coplanar Gas Sensor Arrays. *Sens. Actuators B Chem.* **2010**, *145*, 457–463. [CrossRef]
31. Pedowitz, M.D.; Kim, S.; Lewis, D.I.; Uppalapati, B.; Khan, D.; Bayram, F.; Koley, G.; Daniels, K.M. Fast Selective Sensing of Nitrogen-Based Gases Utilizing δ-MnO_2-Epitaxial Graphene-Silicon Carbide Heterostructures for Room Temperature Gas Sensing. *J. Microelectromechanical Syst.* **2020**, *29*, 846–852. [CrossRef]
32. Alouani, M.A.; Casanova-Chafer, J.; de Bernardi-Martín, S.; García-Gómez, A.; Salehnia, F.; Santos-Ceballos, J.C.; Santos-Betancourt, A.; Vilanova, X.; Llobet, E. The Effect of Doping rGO with Nanosized MnO_2 on Its Gas Sensing Properties. *Chemosensors* **2024**, *12*, 256. [CrossRef]
33. Zhang, H.; Ou, K.; Guan, R.; Cao, Y.; Sun, Y.; Li, X. A Highly Sensitive Room-Temperature NO_2 Gas Sensor Based on Porous MnO_2/rGO Hybrid Composites. *Curr. Nanosci.* **2022**, *19*, 401–409. [CrossRef]
34. Zöpfl, A.; Lemberger, M.-M.; König, M.; Ruhl, G.; Matysik, F.-M.; Hirsch, T. Reduced Graphene Oxide and Graphene Composite Materials for Improved Gas Sensing at Low Temperature. *Faraday Discuss.* **2014**, *173*, 403–414. [CrossRef]
35. Ghosal, S.; Bhattacharyya, P. Fabrication, Characterization, and Gas Sensing Performance of Pd, RGO, and MnO_2 Nanoflowers-Based Ternary Junction Device. *IEEE Trans. Electron. Devices* **2019**, *66*, 3982–3987. [CrossRef]
36. Seara, M.; García, A.; Larraza, I.; Peña, E.; Blanco, V.; Ruiz, S. Method of Obtaining Nanomaterials Composed of Carbonaceous Material and Metallic Oxides. Patent no. ES2678419A1, 25 April 2018.
37. Zhang, Y.; Li, Y.; Jiang, Y.; Duan, Z.; Yuan, Z.; Liu, B.; Huang, Q.; Zhao, Q.; Yang, Y.; Tai, H. Synergistic Effect of Charge Transfer and Interlayer Swelling in V_2CTx/SnS_2 Driving Ultrafast and Highly Sensitive NO_2 Detection at Room Temperature. *Sens. Actuators B Chem.* **2024**, *411*, 135788. [CrossRef]
38. Ahmad, H.; Rahman, M.; Faruki, M.J.; Razalli, S.; Ismail, M.F.; Shah, N.; Razak, M. Graphene Oxide (GO)-Based Wideband Optical Polarizer Using a Non-Adiabatic Microfiber. *J. Mod. Opt.* **2016**, *64*, 439–444. [CrossRef]
39. Yin, F.; Wu, S.; Wang, Y.; Wu, L.; Yuan, P.; Wang, X. Self-Assembly of Mildly Reduced Graphene Oxide Monolayer for Enhanced Raman Scattering. *J. Solid State Chem.* **2016**, *237*, 57–63. [CrossRef]
40. Hurtado, R.; Cortez-Valadez, M.; Aragon-Guajardo, J.R.; Cruz-Rivera, J.; Martinez, F.; Flores-Acosta, M. One-Step Synthesis of Reduced Graphene Oxide/Gold Nanoparticles under Ambient Conditions. *Arab. J. Chem.* **2020**, *13*, 1633–1640. [CrossRef]
41. López Díaz, D.; Delgado Notario, J.; Clerico, V.; Diez, E.; Merchán Moreno, M.D.; Velázquez, M.M. Towards Understanding the Raman Spectrum of Graphene Oxide: The Effect of the Chemical Composition. *Coatings* **2020**, *10*, 524. [CrossRef]
42. Md, S.; Nur, H.; Liu, W.W.; Lai, C.W.; Zulkepli, N.N.; Khe, C.-S.; Hashim, U.; Lee, H.C. Comparison on graphite, graphene oxide and reduced graphene oxide: Synthesis and characterization. *AIP Conf. Proc.* **2017**, *1892*, 150002.
43. Jayashree, M.; Parthibavarman, M.; BoopathiRaja, R.; Sengodan, P.; Ramesh, R. Ultrafine MnO_2/Graphene Based Hybrid Nanoframeworks as High-Performance Flexible Electrode for Energy Storage Applications. *J. Mater. Sci. Mater. Electron.* **2020**, *31*, 6910–6918. [CrossRef]
44. Nadarajan, A.; Kasimayan, U.; Pan, G.-T.; Yang, T.C.-K.; Sharmila, G. One-Pot Synthesis of Covalently Functionalized Reduced Graphene Oxide–Polyaniline Nanocomposite for Supercapacitor Applications. *Clean Technol. Environ. Policy* **2018**, *20*, 2025–2035. [CrossRef]
45. Saadati, F.; Kaboudin, B.; Hasanloei, R.; Namazifar, Z.; Marset, X.; Guillena, G. Manganese Oxide Nanoparticles Supported on Graphene Oxide as an Efficient Nanocatalyst for the Synthesis of 1,2,4-Oxadiazoles from Aldehydes. *Appl. Organomet. Chem.* **2020**, *34*, e5838. [CrossRef]
46. Cantalini, C.; Giancaterini, L.; Treossi, E.; Palermo, V.; Perrozzi, F.; Santucci, S.; Ottaviano, L. *Electrical Response of GO Gas Sensors*; Springer: Berlin/Heidelberg, Germany, 2012. [CrossRef]
47. Donarelli, M.; Prezioso, S.; Perrozzi, F.; Giancaterini, L.; Cantalini, C.; Treossi, E.; Palermo, V.; Santucci, S.; Ottaviano, L. Graphene Oxide for Gas Detection under Standard Humidity Conditions. *2D Mater.* **2015**, *2*, 035018. [CrossRef]

48. Ma, X.; Yuan, Y.; Peng, J.; Mingtai, S.; Chen, Z.; Yin, R.; Su, P.; Wang, X.; Wang, S. High-Performance Gas Sensor Based on GO/In_2O_3 Nanocomposite for Ethanol Detection. *J. Mater. Sci. Mater. Electron.* **2022**, *33*, 15460–15472. [CrossRef]
49. Al-Hartomy, O.; Khasim, S.; Roy, A. Highly Conductive Polyaniline/Graphene Nano-Platelet Composite Sensor towards Detection of Toluene and Benzene Gases. *Appl. Phys. A* **2018**, *125*, 12. [CrossRef]
50. Choudhary, M.; Singh, S.; Sinha, A.K.; Krishnamurthy, S.; Saravanan, K.; Chawla, A.; Avasthi, D.K.; Manna, S.; Chawla, V.; Wadhwa, S. Enhanced Hydrogen Gas Sensing Using Palladium—Graphene Oxide (PdGO) Thin Films. *Chem. Eng. J.* **2024**, *501*, 157604. [CrossRef]
51. Chen, Y.; Zhang, D.; Wang, Z.; Tang, M.; Zhang, H. Pb Transfer-Enabled Recoverable Hydrogel-Based H_2S Colorimetric Sensing with Assistance of Multimodal Deep Learning for Multifunctional Applications. *Adv. Funct. Mater.* **2024**, *34*, 2409017. [CrossRef]
52. Takte, M.; Ingle, N.; Dole, B.; Tsai, M.-L.; Hianik, T.; Shirsat, M. A Stable and Highly-Sensitive Flexible Gas Sensor Based on Ceria (CeO_2) Nano-Cube Decorated rGO Nanosheets for Selective Detection of NO_2 at Room Temperature. *Synth. Met.* **2023**, *297*, 117411. [CrossRef]
53. Fraih, A.; Naeema, N.; Abbas, F. High-Performance NO_2 Gas Sensor Based on Reduced Graphene Oxide/ZrO_2 Hybrids. *J. Met. Mater. Miner.* **2024**, *34*, 2038. [CrossRef]
54. Casanova-Chafer, J.; Ameur, S.; Nsib, M.; Llobet, E. Gas Sensing Properties of Graphene Oxide Loaded with $SrTiO_3$ Nanoparticles. *J. Alloys Compd.* **2023**, *941*, 169011. [CrossRef]
55. Khan, J.; Režo, V.; Vincze, T.; Weis, M.; Momin, S.; El-Atab, N.; Jaafar, M. Flexible and Highly Selective NO_2 Gas Sensor Based on Direct-Ink-Writing of Eco-Friendly Graphene Oxide for Smart Wearable Application. *Chemosphere* **2024**, *367*, 143618. [CrossRef] [PubMed]
56. Mandawade, S.; Wagh, R.; Yewale, C.; Qadir, K.; Abdullah, H.; Alharbi, T.; Husain, D.; Tupe, U.; Naeem, S.; Patil, A. Graphene Oxide Nanoparticles Synthesized via Hummers Method and Investigation of Structural, Electrical, and Gas-Sensing Properties of Screen-Printed Thick Films. *J. Indian Chem. Soc.* **2024**, *102*, 101514. [CrossRef]
57. Kamble, C.; Narwade, S.; Mane, R. Detection of Acetylene (C_2H_2) Gas Using Ag-Modified ZnO/GO Nanorods Prepared by a Hydrothermal Synthesis. *Mater. Sci. Semicond. Process.* **2023**, *153*, 107145. [CrossRef]
58. Akshhayya, C.; Okla, M.; Al-Ghamdi, A.; Abdel-Maksoud, M.; AbdElgawad, H.; Das, A.; Khan, S. Construction of S-Scheme Heterojunction $CuFe_2O_4$/α-MnO_2 with Tuned Bandgap for Enhanced White Light Harvesting: Insights of Photoluminescence, Raman Scattering and Photocatalysis. *Surf. Interfaces* **2021**, *27*, 101523. [CrossRef]
59. Das, P.; Ibrahim, S.; Chakraborty, K.; Ghosh, S.; Pal, T. Stepwise Reduction of Graphene Oxide and Studies on Defect-Controlled Physical Properties. *Sci. Rep.* **2024**, *14*, 294. [CrossRef]
60. Naik, G.; Krishnaswamy, S. Room-Temperature Humidity Sensing Using Graphene Oxide Thin Films. *Graphene* **2016**, *5*, 1–13. [CrossRef]
61. Min, B.K.; Quiller, R.G.; Deiner, L.J.; Friend, C.M. Water Dissociation Associated with NO2 Coadsorption on Mo(110)-(1 × 6)-O: Effect of Coverage and Electronic Properties of Oxygen. *J. Phys. Chem. B* **2005**, *109*, 20463–20468. [CrossRef]